How to cite: *Angew. Chem. Int. Ed.* **2025**, e13903
doi.org/10.1002/anie.202513903

Perovskite Thin Films

Solution ALD of $(CH_3NH_3)(PbI_3)$ Perovskite Thin Films Yields Functional Quality and Stability Superior to Classical Processing

*Vanessa M. Koch[+], Xinyi Zeng[+], Andreas S. Deckert, Pascal Büttner, Evanie Franz, Fei Ding, Michael A. Anderson, Jiyun Zhang, Christian Kupfer, Elena A. Mack, Vipul K. Ambasta, Patrick Duchstein, Katharina E. Dehm, Stevie Furxhiu, Achim Zahl, Johannes Frisch, Felix Hoga, Tobias Stubhan, Regan G. Wilks, Zijian Peng, Olaf Brummel, Ryan W. Crisp, Dirk Zahn, Carolin Müller, Dirk M. Guldi, Marcus Bär, Dorothea Wisser, Jörg Libuda, Christoph J. Brabec, and Julien Bachmann**

Abstract: Atomic-level control of solution-processed hybrid halide perovskites is achieved experimentally by solution atomic layer deposition (sALD). This method transfers the surface chemical principles of gas-phase ALD (gALD) to precursors dissolved in the liquid phase. Circumventing limitations associated with precursor volatility, sALD broadens the portfolio of reaction chemistries usable and material classes accessible. We establish its applicability to depositing ultrathin films of ionic semiconductors by developing an sALD procedure for the most prominent halide perovskite, methylammonium triiodoplumbate ($CH_3NH_3PbI_3$, 'MAPI'). The process saturates upon precursor dosage variation to self-limiting growth typical for ALD, as analyzed by ex-situ and in-situ techniques. sALD-deposited MAPI is highly pure, stoichiometric, and polycrystalline. When MAPI films are prepared in congruent pairs by sALD and by a state-of-the-art spin-coating method, sALD-grown films clearly outperform their spin-coated counterparts in terms of charge carrier lifetimes and stability. They exhibit high carrier mobility and yield functional light absorbing layers in solar cells.

Halide perovskites have established themselves as solar absorbers for photovoltaic (PV) devices with record solar power conversion efficiencies (PCE) > 26%.[1] Not only has their performance skyrocketed,[2] their solution processing offers a comparatively energy-lean and facile access (by spin coating, blade coating, spin casting, drop casting, dip coating, or spray coating).[3–6] These engineering methods, however, do not allow for atomic-scale precision of the individual layer thickness or atomic-scale control of the interfaces between layers. Atomic layer deposition (ALD) delivers such precision

[*] V. M. Koch[+], X. Zeng[+], A. S. Deckert, Dr. P. Büttner, K. E. Dehm, S. Furxhiu, Dr. A. Zahl, Dr. R. W. Crisp, Prof. J. Bachmann
Chemistry of Thin Film Materials, Materials Chemistry section, Department of Chemistry and Pharmacy, Friedrich-Alexander-Universität Erlangen-Nürnberg, IZNF, Cauerstr. 3, 91058 Erlangen, Germany
E-mail: julien.bachmann@fau.de

Dr. E. Franz, F. Ding, Dr. O. Brummel, Dr. D. Wisser, Prof. J. Libuda
Erlangen Center for Interface Research and Catalysis (ECRC), Friedrich-Alexander-Universität Erlangen-Nürnberg, Egerlandstr. 3, 91058 Erlangen, Germany

Dr. M. A. Anderson, Dr. J. Frisch, Dr. R. G. Wilks, Prof. M. Bär
Department of Interface Design, Helmholtz-Zentrum Berlin für Materialien und Energie GmbH (HZB), Albert-Einstein-Str. 15, 12489 Berlin, Germany

J. Zhang, C. Kupfer, F. Hoga, Dr. T. Stubhan, Z. Peng, Prof. C. J. Brabec
Materials for Electronics and Energy Technology, Department of Materials Science and Engineering, Friedrich-Alexander-Universität Erlangen-Nürnberg, Martensstr. 7, 91058 Erlangen, Germany

E. A. Mack, Dr. R. G. Wilks, Prof. D. M. Guldi
Interdisciplinary Center for Molecular Materials (ICMM) & Department of Chemistry and Pharmacy, Friedrich-Alexander-Universität Erlangen-Nürnberg, Egerlandstr. 3, 91058 Erlangen, Germany

V. K. Ambasta, Dr. P. Duchstein, Prof. D. Zahn, Prof. C. Müller
Computer Chemie Centrum, Department of Chemistry and Pharmacy, Friedrich-Alexander-Universität Erlangen-Nürnberg, Nägelsbachstr. 25, 91052 Erlangen, Germany

Prof. M. Bär
Energy Materials In-Situ Laboratory Berlin (EMIL), Helmholtz-Zentrum Berlin für Materialien und Energie GmbH (HZB), Albert-Einstein-Str. 15, 12489 Berlin, Germany

C. Kupfer, Prof. M. Bär
Department of Chemistry and Pharmacy, Friedrich-Alexander-Universität Erlangen-Nürnberg, Egerlandstr. 3, 91058 Erlangen, Germany

Prof. M. Bär
Helmholtz-Institute Erlangen-Nürnberg for Renewable Energy (HIERN), Albert-Einstein-Str. 15, 12489 Berlin, Germany

[+] Both authors contributed equally to this work.

Additional supporting information can be found online in the Supporting Information section

and control by exploiting self-terminating surface chemical reactions of two (or more) precursors to provide sequentially the individual elements constituting the solid. In this thin film deposition technique, precursors with programmed reactivity alternate in their reactions with the solid surface of a substrate avoiding direct contact with each other. Repeating this alternation in a cyclic manner delivers a thin film with high conformality even in structures of high aspect ratio.[7] However, the vacuum processing of classical ALD demands that precursors be volatile. Since halide perovskites consist of separate ions, they have remained inaccessible by ALD so far. Thus, perfectly conformal, nanometer-precise coatings of these ionic solids have not been achieved to date.

The invention of solution atomic layer deposition (sALD) offers new opportunities.[8,9] sALD transfers the principles of classical gas-phase ALD (gALD) into the solution processing field and expands the possibilities of the broader atomic-layer processing field. It offers a more facile practical implementation, a wider range of precursors, including ionic ones, and a broad portfolio of reactivity types that can be exploited. Processing conditions as mild as room temperature and atmospheric pressure can deliver, in sALD mode, materials of high purity and crystalline quality. Beyond oxides,[8] heavier chalcogenides,[10–12] hydrides,[13] metal–organic frameworks (MOFs),[14] and polymers are accessible by sALD.[15] This work establishes the sALD processing of the prototypical member of the hybrid halide perovskite family (methylammonium triiodoplumbate, $(CH_3NH_3)(PbI_3)$, also referred to as methylammonium lead iodide, 'MAPI'), and we demonstrate that the atomic-level control afforded by sALD leads, in a single processing step, to a material of outstanding purity, of improved stability, and of superior functional performance.

To achieve sALD growth, the product $(CH_3NH_3)(PbI_3)$ must be insoluble in the chosen solvent, in contrast to the ionic precursors delivering each component of it. Methylammonium iodide, $(CH_3NH_3)I$, provides moderate solubility in chloroform spiked with alcohol. The pivalate complex $Pb(Piv)_2$ serves as an adequate source of lead(II) thanks to organic ligands that provide solubility in chloroform and prevent aggregation by chelation but remain sufficiently labile, enabling ion pair separation. The sALD process envisioned (Figure 1a) relies on excess surface charge the sign of which alternates with individual reaction steps.

The initial steps of sALD nucleation on (110) SnO_2 and growth are simulated through molecular dynamics (MD, Figure 1b,c). First, lead ions from $Pb(Piv)_2$ bind to protruding surface oxides to initiate a contact layer while pivalates build salt bridges to Sn^{4+}. In the next step introducing three equivalents of $(CH_3NH_3)I$, most ions remain in a dynamic interaction with the surface, until iodides exchange pivalates to generate persistent Pb–I–Pb motifs characteristic for the (100) layer of MAPI. Extended relaxation yields a stable interface model featuring Pb—I distances of ~3.75 Å akin to the MAPI (100) layer. Based on this MD-derived interface model, density functional theory (DFT) calculation of a (001)-oriented cubic MAPI supercell (2 × 2) aligned in x and y with the SnO_2 (110) lattice yields in initial monolayer structure (Figure 1d, yellow) exhibiting an average nearest-neighbor Pb···Pb distance of 6.38 Å. Upon sequential addition of layers, the Pb···Pb distances decrease consistently (values in Figure 1d), indicating progressive structural relaxation toward the bulk structure (~6.00 Å). Adsorption energies are thermodynamically favorable, decrease with increasing layer number, but imply stability beyond three layers.

To realize this growth plan on SnO_2 (common charge transport layer in perovskite photovoltaics based on its favorable energy level alignment),[16] the initial pre-treatment involves cleaning with UV/ozone followed by exposures to KCl and $Pb(Piv)_2$ as aqueous and chloroform solutions, respectively (Figure S1).[17,18] After rinsing with chloroform, the sALD steps involve (at room temperature): 1) $(CH_3NH_3)I$ 4 mM pulse, 2) rinse, 3) $Pb(Piv)_2$ 1 mM pulse, 4) rinse. Repeating these four steps results in the accretion of an increasingly dark brown film also evidenced by spectroscopic ellipsometry, Figure 1e,f. Thickness quantification by ellipsometry and field-emission scanning electron microscopy (FE–SEM) in cross-section indicates linear growth with 1.2 nm added per sALD cycle performed (Figure 1f), consistent with the size of the MAPI unit cell.[19] The self-limiting nature of each surface reaction (the hallmark of ALD) is demonstrated by varying the dosage of both precursors (Figure 1g): beyond the standard 10-s pulse duration, the growth per cycle (GPC) reaches a plateau.

The chemical identity of the film is provided by x-ray diffraction in grazing incidence (GIXRD, Figure 2a). Despite the mild operation conditions of our sALD procedure, the MAPI films are crystalline as deposited, without any subsequent thermal or solvent annealing step. The diffractogram of a MAPI film obtained after 30 sALD cycles on SnO_2 features the reflexes of tetragonal $(CH_3NH_3)(PbI_3)$. Importantly, no signal of PbI_2 (a typical degradation product and impurity) is present at 12.7°, hinting at not only the purity but also the unusual stability of the sALD-derived MAPI exposed to moist air and x-rays (4 h). Atomic force micrographs (AFM) and FE–SEM of MAPI deposits evidence that in the initial stages of growth, the solid is a homogeneously distributed but granular film, exhibiting crystallites which become densely packed after some tens of cycles (Figure 2b–e). After 120 cycles, the nuclei have merged into a continuous layer of dense crystals (Figure 2f), although some voids remain between the SnO_2 and MAPI layers. This behavior is in line with previous sALD studies in which a rougher and more granular structure has been observed than in more ideal gALD cases,[11,12] and it represents an improvement over previous MAPI processing methods, which cannot deliver continuous films of such low thickness.[20–23] Maximizing the number of nucleation sites delivers the best possible adhesion but does not inhibit the surface mobility of adsorbates. This mobility enables the formation of a crystalline deposit but also tends to increase the surface roughness.[12]

Qualitative elemental analysis by energy dispersive x-ray analysis (EDX, Figure 3a) confirms the presence of the expected elements C, N, Pb, I, Sn, O, and Si. Element quantification by x-ray photoelectron spectroscopy (XPS, survey scan Figure 3b) demonstrates via the absence of Sn signal that after 70 sALD cycles, the MAPI layer is already closed. Moreover, the XPS-derived C:N:Pb:I composition (1.5/0.9/1.0/3.6) is very close to the nominal composition

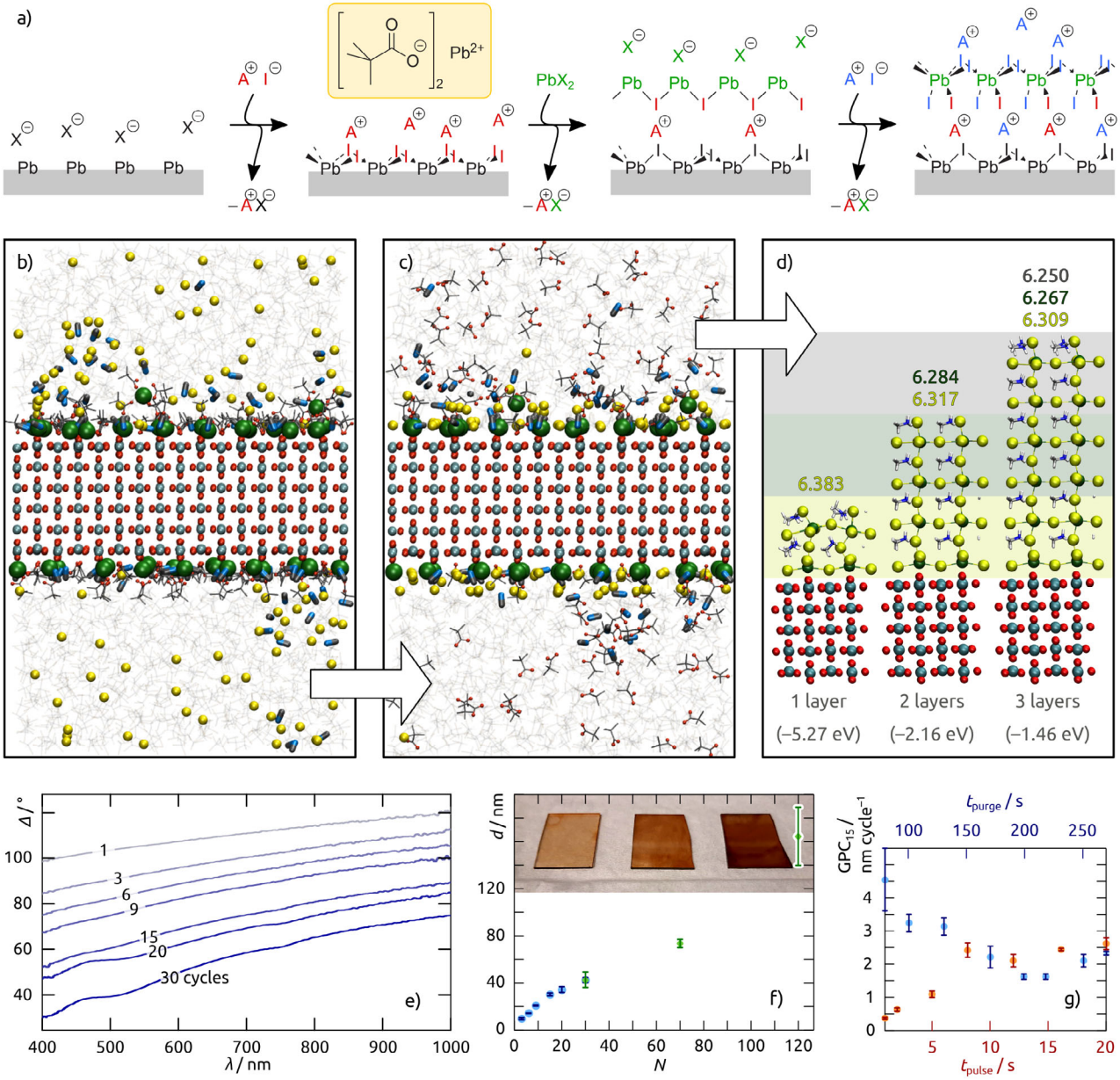

Figure 1. MAPI sALD growth chemistry. a) Schematic presentation of the design with A^+ = methylammonium and X^- = pivalate (yellow frame). Each step in the reaction binds alternating ions (1.5 cycles shown). b) and c) MD simulation of nucleation in the first sALD cycle upon exposure of SnO_2 to $Pb(Piv)_2$ then $(H_3CNH_3)I$. d) DFT computation of the structures of MAPI films obtained after one, two, and three cycles (binding energies and average Pt···Pt distances in Å indicated below and above, respectively). e) Experimental observation of growth on a SnO_2-coated Si/SiO_2 wafer by spectroscopic ellipsometry (orientation $\Delta(\lambda)$) after N sALD cycles, $N = 1$ to 30. f) Determination of the growth rate by spectroscopic ellipsometry (blue datapoints) and SEM (green), optical appearance of quartz substrate coated with 20, 40, and 60 cycles. g) Demonstration of self-limiting growth by varying the duration of precursor exposure and solvent purge at each cycle.

(1/1/1/3). Beyond the usual surface contamination by adventitious C, the 20% extra amount of iodine obtained after the last sALD pulse of methylammonium iodide is in line with the growth mechanism detailed in Figure 1. The individual core level regions Pb 4f, I 3d, N 1s, and C 1s consistently provide evidence for the extraordinary quality of the sample, with all signals (Pb $4f_{7/2}$, 138.7 eV; Pb $4f_{5/2}$, 143.5 eV; I $3d_{5/2}$, 619.6 eV; I $3d_{3/2}$, 631.1 eV; N 1 s, 402.6 eV; C 1 s, 286.7 eV, Figure 3b–f) all supporting the presence of MAPI,[24–26] and the absence of any secondary phase. These unusually clean XPS analyses confirm that the high material quality is maintained under prolonged vacuum and x-ray exposure (further elaborated on below), a feature which is unusual for the rather labile MAPI,[24,27] but which fits with the stability already noted in GI–XRD measurements above.

Can the mechanism put forth in Figure 1 be confirmed experimentally? Infrared spectroscopy in attenuated total reflection (ATR-IR) performed in situ during MAPI sALD in an ATR flow cell evidences the appearance of the most intense signals characteristic of the MAPI solid after the

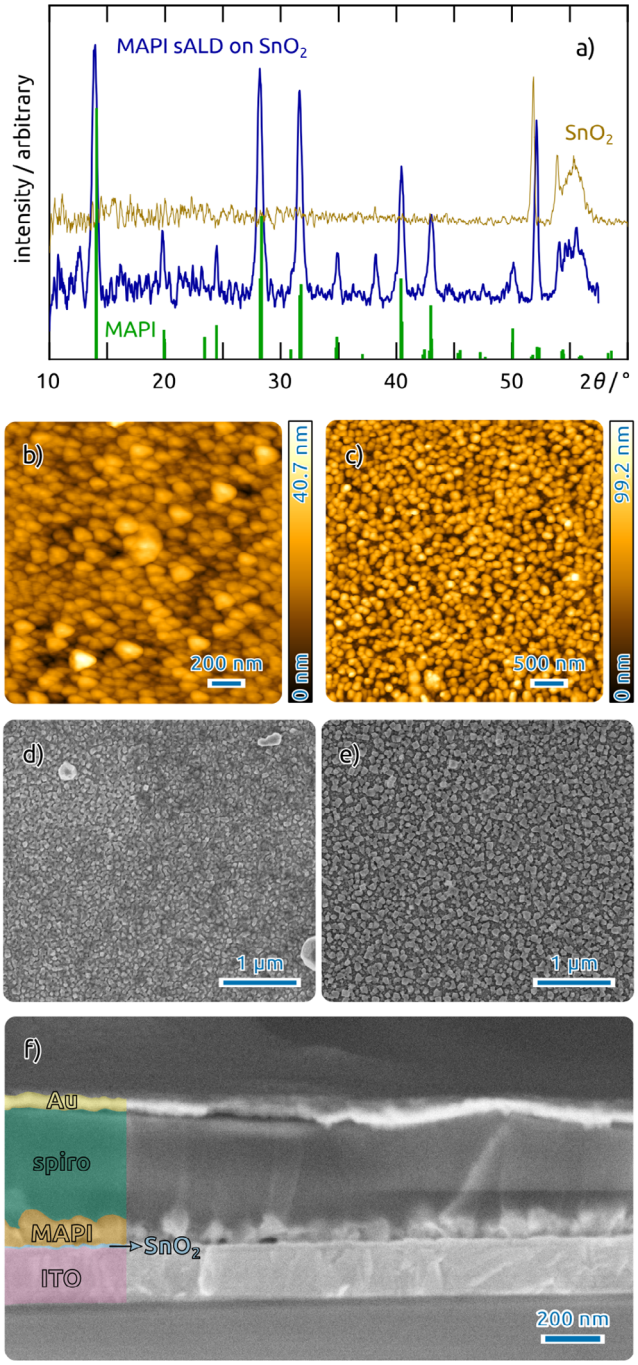

Figure 2. Structural characterization of sALD MAPI films. a) GIXRD diffractogram of an as-grown sample featuring 30 MAPI sALD cycles on a SnO_2-coated Si/SiO_2 wafer piece (blue), compared to a bare substrate (beige) and a reference (COD no. 721893, green bars). b) and c) AFM micrographs of MAPI films obtained after 9 and 30 sALD cycles, respectively. d) SEM micrographs after 15 and 60 cycles. e) SEM cross-section of a functional photovoltaic stack consisting of glass / 200 nm ITO / 15 nm SnO_2 (gALD) / 120 cycles MAPI (sALD) / 400 nm spiro-OMeTAD ("spiro", spin coating) / 80 nm Au (evaporated).

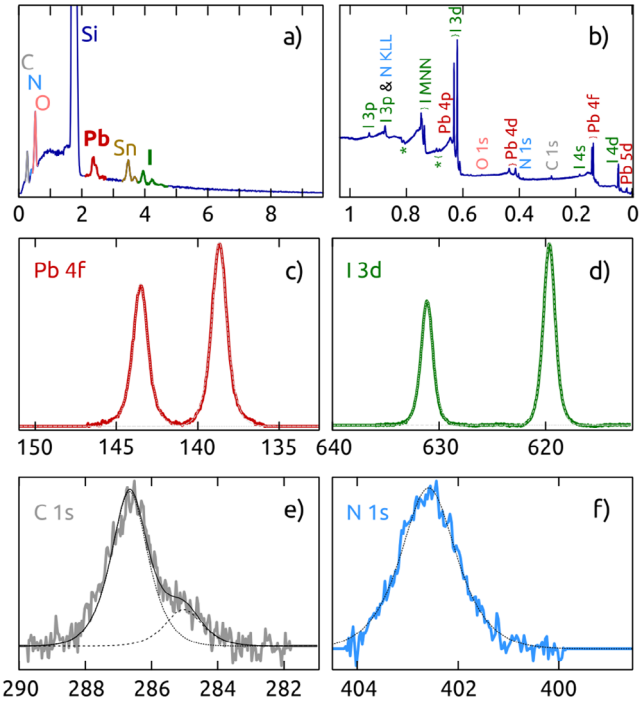

Figure 3. Chemical composition of sALD-grown MAPI films. a) EDX microanalysis of a film obtained after 30 cycles MAPI sALD on SnO_2. b)–f)XPS spectra of a film obtained after 70 cycles, including a survey spectrum and the core level regions of Pb 4f, I 3d, C 1s, and N 1s.

very first cycle already (Figure 4a,b). Subsequent cycles cause a stepwise increase in all bands associated with MAPI at 3186 cm^{-1} ($\nu_{as}(NH_3^+)$), 3140 cm^{-1} ($\nu_s(NH_3^+)$), 1579 cm^{-1} ($\delta(NH_3^+)$), 1470 cm^{-1} ($\delta(CH_3\text{-}NH_3^+)$), 1423 cm^{-1} ($\delta(CH_3)$).[28–31] Spurious negative signals at 1215 cm^{-1} are attributed to the solvent.[32] Thus, nucleation is immediate and growth occurs linearly (see also Figure S2). The $\delta(CH_3\text{–}NH_3^+)$ band provides further insight into the initial stages of deposition. Indeed, its maximum blue-shifts by approximately 1 cm^{-1} during the first five to ten cycles, Figure 4c. This shift corresponds to the transition from isolated clusters with rather molecular nature on the surface to an extended MAPI solid at quite early stages of growth. The UV–visible absorption spectra (Figure 4d) corroborate that the semiconductor band structure of MAPI is fully formed as a sharp absorption edge near 780 nm (bandgap 1.58 eV based on the Tauc method,[33,34] in agreement with the literature)[35,36] in the thinnest sample measured (20 cycles). This edge does not shift in later stages of growth.

A molecular picture of the nucleation reaction is provided on quartz wool (SiO_2) by solid-state magic angle spinning proton nuclear magnetic resonance (^1H MAS NMR) measurements (Figure S3). After an initial solvent exposure, the support shows resonances for SiOH groups at 1.8 ppm and some adsorbed water (3.5–4.0 ppm). New signals appear after the first cycle, which can be attributed to adsorbed solvents chloroform (7.6 ppm) and isopropanol (1.1 ppm). The signal associated with the nitrogen-bound protons of adsorbed methylammonium at 6.2 ppm appears after the very first cycle already, in line with the observations by ATR-IR.

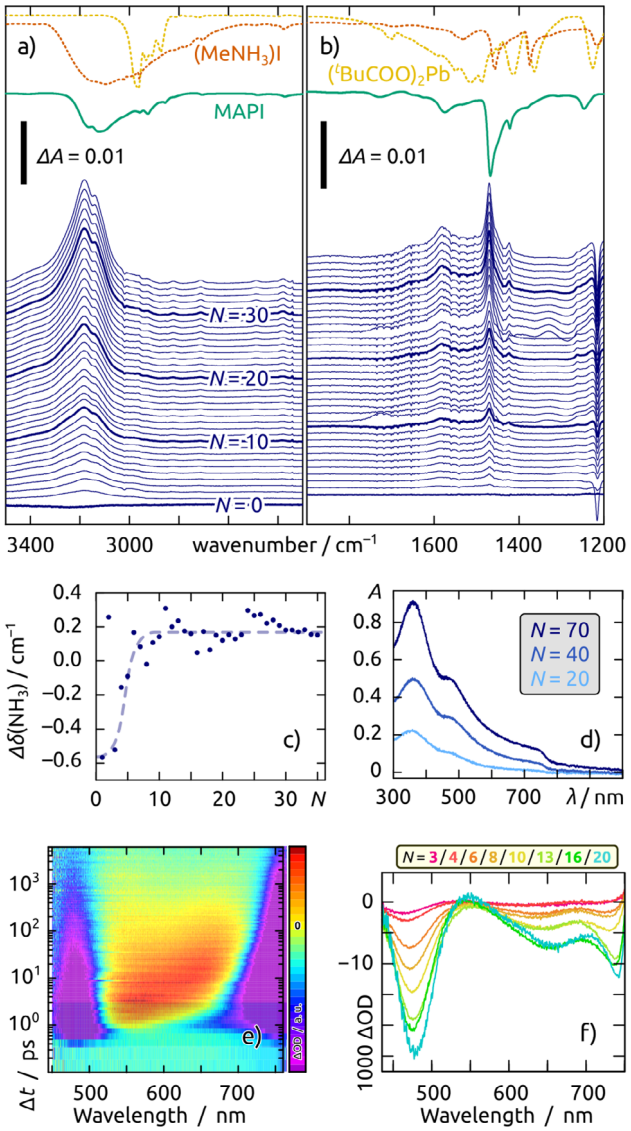

Figure 4. Characterization of nucleation and growth mechanism. a) and b) ATR-IR spectra recorded during the first 35 cycles of MAPI sALD process inside a flow cell. The reference transmission spectra measured of $Pb(Piv)_2$, $(CH_3NH_3)I$, and MAPI are shown in the top part in yellow, orange and green, respectively. The ordinate axis scale bar represents $\Delta A = 0.01$. c) Shift of the $\delta(CH_3\text{-}NH_3^+)$ band position versus number N of sALD cycles. The ordinate axis is referenced to 1470 cm^{-1}. d) UV–vis absorption spectra of MAPI films obtained after $N = 20$, 40, and 70 sALD cycles on a quartz substrate. e) Exemplary transient absorption spectroscopy (TAS) dataset collected of the sALD MAPI film in situ during growth, specifically after 20 cycles, upon excitation at 400 nm. f) Exemplary evolution-associated spectra (EAS) extracted for the first identified transient state from the in-situ datasets collected after various numbers N of sALD cycles.

After 12 cycles, both resonances associated with methylammonium (3.2 and 6.2 ppm) are clearly visible. Comparison of the spectrum with a MAPI single crystal allows for the unambiguous assignment of the solid formed, whereas the narrow line width indicates a high degree of order.

How thin can a functional semiconductor film generated by sALD be? An in-situ study by ultrafast pump-probe transient absorption spectroscopy (TAS, Figure 4e,f and Figure S4) yields interpretable datasets after 3 sALD cycles, and between 3 and 20 cycles all datasets can be fitted with one common model of four sequential, exponential decays from the originally formed excited state associated with EAS1 to EAS2, EAS3, and the last state observable on the TAS timescales, EAS4 (Figure S4a–d). The lifetimes are on the order of 2, 5, 75 ps, and 2 ns, respectively, without obvious trends as they depend on the number N of sALD cycles performed. The fast processes are likely associated with hot carrier thermalization, whereas carrier trapping happens on the longer timescales. In the absence of charge collection to external electrodes, carriers then recombine slowly. Interestingly, the evolution-associated spectra (EAS) extracted from this analysis exhibit systematic changes with N. Not only do the signal intensities scale with the layer thickness as expected, the extrema also shift significantly. This is particularly true of the blue-region bleach exhibited by the originally formed excited state (EAS1, Figures 4f and S4a), which red-shifts by more than 10 nm from $N = 3$ to $N = 20$, a manifestation of quantum confinement of the carriers photogenerated in the nanometer-sized clusters generated in the first few sALD cycles, before the properties of the bulk solid are reached. These observations draw a picture consistent with the in-situ ATR-IR and MAS NMR data.

Let us now determine how the well-defined and immediate heterogeneous nucleation demonstrated above affects the functional properties of our sALD-deposited MAPI films. Hall effect measurements performed on as-grown MAPI (120 cycles on quartz) under ambient conditions without irradiation (Figure S5) indicate the semiconductor to be p-type.[37] The charge carrier concentration of $1.9 \bullet 10^{10}$ cm^{-3} evidences an extraordinarily intrinsic semiconductor.[38] The extremely high mobility 1200 $cm^2\ V^{-1}\ s^{-1}$ is very close to the theoretical values 1500–5500 $cm^2\ V^{-1}\ s^{-1}$ recently computed.[39] This superior semiconductor quality also appears in time-resolved photoluminescence spectroscopy (TR-PL). The luminescence decay datasets recorded under ambient conditions of a comparative set of different MAPI film thicknesses (40, 80, and 170 nm) prepared by sALD and by traditional spin coating (Figure 5) evidence significantly longer charge carrier recombination lifetimes for sALD films than their traditionally prepared counterparts (spin-coating with state-of-the-art procedure) for each thickness tested, on a rare microsecond timescale.[40]

The material quality is complemented by a stability unheard of for MAPI films so far. Often, perovskites exhibit organic cation loss and formation of metallic lead when stressed by high intensity x-rays in the vacuum conditions of an XPS instrument.[41–43] A comparative quantification of degradation under x-ray irradiation and/or vacuum conditions of spin-coated MAPI samples with sALD films (Figure S6) shows methylamine loss under high X-ray power (300 W) for both spin-coated and sALD samples, but at a rate significantly larger for the former (21% and 41% after 6 and 12 h, versus 8.4% and 13% for sALD MAPI). A Pb(0) peak increases to 8.0% with exposure of the spin-coated film, but remains conspicuously absent from the sALD film spectrum. The vacuum stability of the films contrasts only a 14% loss in MA^+ intensity after 5 days with 37% for the spin-coated sample.

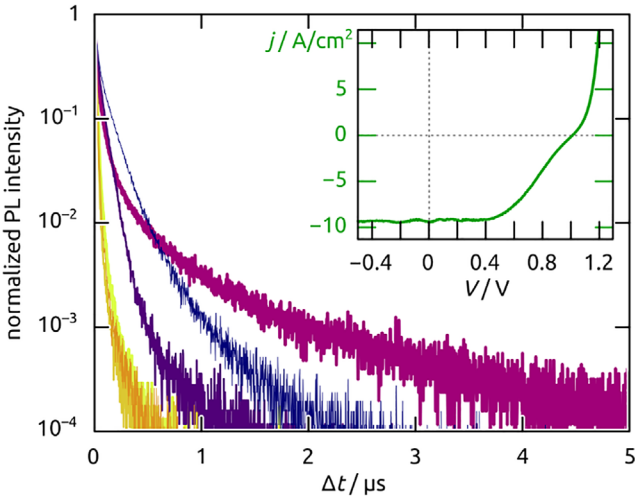

Figure 5. Opto-electronic properties of sALD MAPI films. (Main) TR-PL traces (excitation wavelength 402 nm) of MAPI films deposited by sALD (purple to blue shades: raspberry 40 nm, grape 80 nm, and marine blue 170 nm) and by spin coating (yellow to ocher shades, strongly overlapping: green–yellow 40 nm, mustard 80 nm, and tangerine 170 nm) on glass. The datasets are rendered comparable in pairs of similar thicknesses. (Inset) Solar cell performance: *j*–*V* reverse scan (one sun, scan speed 50 mV s^{-1}, step size 2 mV) of the champion cell with a contact area of 0.1475 cm^2.

Similar conclusions are reached when the stability of MAPI films (sALD / spin-coated) is quantified by photoluminescence (PL) during 144 h under the usual ambient stress factors: room (humid) air, elevated temperature, and simulated solar light irradiation (Figure S7).[44] In air, for example, the sALD film retains more than 75% of its initial photoluminescence (PL) intensity after the 144-h test, whereas the spin-coated film has lost most of its PL activity, having decayed to below 6%.

The opto-electronic properties of the material translate into functional device performance. Solar cells made with MAPI films by sALD and characterized under ambient conditions without any further protection or precautions yield open-circuit voltage values (V_{oc}) of up to 1.00 V along the reverse *j*–*V* curve (Figure 5 inset, measured from −0.5 V to +1.2 V) for the champion cell (planar stack: glass / 200 nm ITO / 30 nm SnO_2 / 137 cycles MAPI / 400 nm spiro-OMeTAD / 80 nm Au, Figure S8). This value is comparable to performance reported in the literature with much thicker spin-coated MAPI films.[45,46] A decent current density *j* of 9.11 mA cm^{-2} and a rather low fill factor (FF) of 45% yield an overall solar power conversion efficiency (PCE) of 4.2%. External and internal quantum efficiency spectra (EQE, IQE) indicate that charge carriers are generated in the planar device throughout the visible range (Figure S9) and imperfectly extracted, reflected in the somewhat triangular shape of the spectrum.[47,48] This indicates a suboptimal interface engineering of the PV stack. Therefore, our unusually thin sALD-grown MAPI itself exhibits semiconductor performance on par with the much thicker films derived from more classical solution processing methods.

In conclusion, the invention of ALD from precursors dissolved in liquid phases ('solution ALD', sALD) opens the field of atomic-scale processing to novel families of precursors and chemistries, enabling access to materials which had remained out of reach of ALD processing,[8,14,15] and offering an avenue toward applications to non-planar substrates (Figure S10). Ionic solids belong to those material types where a general strategy toward delivering building blocks from the gas phase is difficult to envision. The results presented here prove the validity of the sALD method and its usefulness in the field of hybrid halide perovskites, as it has enabled the first direct atomic-scale deposition process of methylammonium triiodoplumbate ("methylammonium lead iodide", MAPI).

The methodology developed here demonstrates important advances for the perovskite semiconductor field. First, ALD delivers a level of control that traditional processing based on the evaporation of inks cannot achieve. The thickness of the coating can be adjusted accurately and uniformly even on non-planar substrates. Second, ALD relies on a purely heterogeneous nucleation, that is, the new solid phase is started exclusively on the surface of the substrate and not by aggregation of building blocks dissolved or suspended within the liquid phase. This means that chemical bonding between the substrate and the film is optimal, and adhesion maximized. Interface defects are avoided, which otherwise cause recombination of carriers and serve as nucleation points for decomposition. In other words, controlling nucleation of the new phase on the substrate at the level of individual ions results in significantly improved stability, structural quality, and functional performance.

In concrete terms, our approach validated on the most prototypical hybrid halide perovskite "MAPI" can be chemically followed in situ with a precision down to individual ionic layers by ATR-IR, MAS NMR, and TAS spectroscopies. Together, these complementary methods demonstrate convincingly that nucleation is immediate and that after only individual cycles it yields a material of correct chemical identity but as clusters electronically isolated from each other. After further deposition, the resulting layers yield outstanding carrier mobilities and lifetimes and allow for building devices with a high V_{oc} of 1.0 V in a simple semiconductor stack, on par with the very best examples to date.

Supporting Information

The authors have cited additional references within the Supporting Information.[48–74] All raw data have been made available on the Zenodo platform: https://zenodo.org/records/17116673.

Acknowledgements

The authors thank Laura Progscha for her support with references formatting. This work was funded by Deutsche Forschungsgemeinschaft (German Research Foundation, DFG) within the Collaborative Research Center 'ChemPrint' (project 538767711, CRC 1719). D.W. and F.D. gratefully acknowledge financial support by the DFG via the core

facility Erlangen Center for Functional Particle Systems (project-ID 539724755) and the grant WI-4934/3–1 (project-ID 503810318). M.A.A. acknowledges financial support from the Fully Connected Virtual and Physical Perovskite Photovoltaic Lab (VIPERLAB) project. The authors are grateful to the Energy Materials In-situ Laboratory Berlin (EMIL) for making the infrastructure to perform XPS measurements available. K.E.D. acknowledges scholarship funding from the *Deutsche Bundesstiftung Umwelt* (DBU – German Federal Environmental Foundation).

Open access funding enabled and organized by Projekt DEAL.

Conflict of Interests

The authors declare no conflict of interest.

Data Availability Statement

The data that support the findings of this study are openly available in Zenodo at https://zenodo.org/records/17116673, 17116673.

Keywords: Chemical vapor deposition · Crystal growth · Perovskites · Semiconductors · Thin films

[1] F. Ma, Y. Zhao, Z. Qu, J. You, *Acc. Mater. Res.* **2023**, *4*, 716–725, https://doi.org/10.1021/accountsmr.3c00068.
[2] National Renewable Energy Laboratory (NREL), "Best Research-Cell Efficiencies", can be found under https://www.nrel.gov/docs/libraries/pv/best-research-cell-efficiencies.pdf?sfvrsn=26e2254e_9, 2025 (accessed on 27.05.2025).
[3] A. Olaleru, E. Maluta, J. Kirui, O. Adekoya, in *Thin Films Photovoltaics* (Eds.: B. Zaidi, C. Shekhar), IntechOpen, London **2022**, https://doi.org/10.5772/intechopen.96073.
[4] Z. Yang, C.-C. Chueh, F. Zuo, J. H. Kim, P.-W. Liang, A. K.-Y. Jen, *Adv. Energy Mater.* **2015**, *5*, 1500328, https://doi.org/10.1002/aenm.201500328.
[5] M. L. Petrus, J. Schlipf, C. Li, T. P. Gujar, N. Giesbrecht, P. Müller-Buschbaum, M. Thelakkat, T. Bein, S. Hüttner, P. Docampo, *Adv. Energy Mater.* **2018**, *8*, 1703396, https://doi.org/10.1002/aenm.201703396.
[6] C. Lan, Z. Zhou, R. Wei, J. C. Ho, *Mater. Today Energy* **2019**, *11*, 61–82, https://doi.org/10.1016/j.mtener.2018.10.008.
[7] R. L. Puurunen, *J. Appl. Phys.* **2005**, *97*, 121301, https://doi.org/10.1063/1.1940727.
[8] Y. Wu, D. Döhler, M. Barr, E. Oks, M. Wolf, L. Santinacci, J. Bachmann, *Nano Lett.* **2015**, *15*, 6379–6385, https://doi.org/10.1021/acs.nanolett.5b01424.
[9] O. Graniel, J. Puigmartí-Luis, D. Muñoz-Rojas, *Dalton Trans.* **2021**, *50*, 6373–6381, https://doi.org/10.1039/D1DT00232E.
[10] Y. Cao, S. Zhu, J. Bachmann, *Dalton Trans.* **2021**, *50*, 13066–13072, https://doi.org/10.1039/D1DT01232K.
[11] V. M. Koch, M. K. S. Barr, P. Büttner, I. Mínguez-Bacho, D. Döhler, B. Winzer, E. Reinhardt, D. Segets, J. Bachmann, *J. Mater. Chem. A.* **2019**, *7*, 25112–25119, https://doi.org/10.1039/C9TA09715E.
[12] V. M. Koch, J. Charvot, Y. Cao, C. Hartmann, R. G. Wilks, I. Kundrata, I. Mínguez-Bacho, N. Gheshlaghi, F. Hoga, T. Stubhan, W. Alex, D. Pokorný, E. Topraksal, A.-S. Smith, C. J. Brabec, M. Bär, D. M. Guldi, M. K. S. Barr, F. Bureš, J. Bachmann, *Chem. Mater.* **2022**, *34*, 9392–9401, https://doi.org/10.1021/acs.chemmater.2c01550.
[13] I. Kundrata, K. Fröhlich, L. Vančo, M. Mičušík, J. Bachmann, *Beilstein J. Nanotechnol.* **2019**, *10*, 1443–1451, https://doi.org/10.3762/bjnano.10.142.
[14] M. K. S. Barr, S. Nadiri, D.-H. Chen, P. G. Weidler, S. Bochmann, H. Baumgart, J. Bachmann, E. Redel, *Chem. Mater.* **2022**, *34*, 9836–9843, https://doi.org/10.1021/acs.chemmater.2c01102.
[15] J. Fichtner, Y. Wu, J. Hitzenberger, T. Drewello, J. Bachmann, *ECS J. Solid State Sci. Technol.* **2017**, *6*, N171–N175, https://doi.org/10.1149/2.0291709jss.
[16] P. Wu, S. Wang, X. Li, F. Zhang, *J. Mater. Chem. A.* **2021**, *9*, 19554–19588, https://doi.org/10.1039/D1TA04130D.
[17] X. Liu, Y. Zhang, L. Shi, Z. Liu, J. Huang, J. S. Yun, Y. Zeng, A. Pu, K. Sun, Z. Hameiri, J. A. Stride, J. Seidel, M. A. Green, X. Hao, *Adv. Energy Mater.* **2018**, *8*, 1800138, https://doi.org/10.1002/aenm.201800138.
[18] M. Hou, Y. Wang, M. Han, H. Ren, R. Wang, J. Zhao, Q. Huang, Y. Ding, X. Zhang, G. Hou, Y. Zhao, *Org. Electron.* **2022**, *106*, 106527, https://doi.org/10.1016/j.orgel.2022.106527.
[19] T. Oku, Crystal Structures of $CH_3NH_3PbI_3$ and Related Perovskite Compounds Used for Solar Cells" in *Solar Cells - New Approaches and Reviews* (Ed.: L. A. Kosyachenko), IntechOpen, London **2015**.
[20] Y. Zhou, M. Yang, A. L. Vasiliev, H. F. Garces, Y. Zhao, D. Wang, S. Pang, K. Zhu, N. P. Padture, *J. Mater. Chem. A.* **2015**, *3*, 9249–9256, https://doi.org/10.1039/C4TA07036D.
[21] P. Fan, D. Gu, G.-X. Liang, J.-T. Luo, J.-L. Chen, Z.-H. Zheng, D.-P. Zhang, *Sci. Rep.* **2016**, *6*, 29910, https://doi.org/10.1038/srep29910.
[22] D. Y. Torres-Martínez, M. Millán, B. Aguilar, O. Navarro, *Phys. B : Condens. Matter.* **2020**, *585*, 412081, https://doi.org/10.1016/j.physb.2020.412081.
[23] A. Kumar, M. Shkir, H. H. Somaily, K. L. Singh, B. C. Choudhary, S. K. Tripathi, *Phys. B: Condens. Matter.* **2022**, *630*, 413678, https://doi.org/10.1016/j.physb.2022.413678.
[24] C. Das, M. Wussler, T. Hellmann, T. Mayer, W. Jaegermann, *Phys. Chem. Chem. Phys.* **2018**, *20*, 17180–17187, https://doi.org/10.1039/C8CP01259H.
[25] Z. Hawash, S. R. Raga, D.-Y. Son, L. K. Ono, N.-G. Park, Y. Qi, *J. Phys. Chem. Lett.* **2017**, *8*, 3947–3953, https://doi.org/10.1021/acs.jpclett.7b01508.
[26] L. Liu, J. A. McLeod, R. Wang, P. Shen, S. Duhm, *Phys. Lett.* **2015**, *107*, 061904.
[27] J. D. McGettrick, K. Hooper, A. Pockett, J. Baker, J. Troughton, M. Carnie, T. Watson, *Mater. Lett.* **2019**, *251*, 98–101, https://doi.org/10.1016/j.matlet.2019.04.081.
[28] Z. Zhu, V. G. Hadjiev, Y. Rong, R. Guo, B. Cao, Z. Tang, F. Qin, Y. Li, Y. Wang, F. Hao, S. Venkatesan, W. Li, S. Baldelli, A. M. Guloy, H. Fang, Y. Hu, Y. Yao, Z. Wang, J. Bao, *Chem. Mater.* **2016**, *28*, 7385–7393, https://doi.org/10.1021/acs.chemmater.6b02883.
[29] M. Acik, T. M. Alam, F. Guo, Y. Ren, B. Lee, R. A. Rosenberg, J. F. Mitchell, I. K. Park, G. Lee, S. B. Darling, *Adv. Energy Mater.* **2018**, *8*, 1–14, https://doi.org/10.1002/aenm.201701726.
[30] Y. Wen, G. Zhu, Y. Shao, *J. Mater. Sci.* **2020**, *55*, 2937–2946, https://doi.org/10.1007/s10853-019-04145-9.
[31] M. A. Pérez-Osorio, R. L. Milot, M. R. Filip, J. B. Patel, L. M. Herz, M. B. Johnston, F. Giustino, *J. Phys. Chem. C.* **2015**, *119*, 25703–25718, https://doi.org/10.1021/acs.jpcc.5b07432.
[32] T. G. Gibian, D. S. McKinney, *J. Am. Chem. Soc.* **1951**, *73*, 1431–1434, https://doi.org/10.1021/ja01148a009.

[33] J. Tauc, R. Grigorovici, A. Vancu, *Phys. Stat. Sol.* **1966**, *15*, 627–637, https://doi.org/10.1002/pssb.19660150224.

[34] G. G. Valle, P. Hammer, S. H. Pulcinelli, C. V. Santilli, *J. Eur. Ceram. Soc.***2004**, *24*, 1009–1013, https://doi.org/10.1016/S0955-2219(03)00597-1.

[35] W. Huang, Y. Liu, S. Yue, L. Zhu, P. Jin, Q. Wu, Y. Zhang, S. Qu, Z. Wang, Y. Chen, *Sci. China Technol.* **2018**, *61*, 886–892, https://doi.org/10.1007/s11431-017-9211-6.

[36] M. Filipič, P. Löper, B. Niesen, S. De Wolf, J. Krc, C. Ballif, M. Topic, *Opt. Express* **2015**, *23*, A263–A278.

[37] Q. Wang, Y. Shao, H. Xie, L. Lyu, X. Liu, Y. Gao, J. Huang, *Appl. Phys. Lett.* **2014**, *105*, 163508, https://doi.org/10.1063/1.4899051.

[38] W. Zhou, Y. Chen, H. Zhou, *Acta Phys.-Chim. Sin.* **2021**, *37*, 2009044.

[39] C. C. Stoumpos, C. D. Malliakas, M. G. Kanatzidis, *Inorg. Chem.* **2013**, *52*, 9019–9038, https://doi.org/10.1021/ic401215x.

[40] Q. Dong, Y. Fang, Y. Shao, P. Mulligan, J. Qiu, L. Cao, J. Huang, *Science* **2015**, *347*, 967–970.

[41] W.-C. Lin, W.-C. Lo, J.-X. Li, Y.-K. Wang, J.-F. Tang, Z.-Y. Fong, *npj Mater. Degrad.* **2021**, *5*, 13, https://doi.org/10.1038/s41529-021-00162-9.

[42] S. Svanström, A. García-Fernández, T. Sloboda, T. J. Jacobsson, H. Rensmo, U. B. Cappel, *Phys. Chem. Chem. Phys.* **2021**, *23*, 12479–12489, https://doi.org/10.1039/D1CP01443A.

[43] A. García-Fernández, B. Kammlander, S. Riva, H. Rensmo, U. B. Cappel, *Phys. Chem. Chem. Phys.* **2024**, *26*, 1000–1010, https://doi.org/10.1039/D3CP05061K.

[44] Z. Peng, J. Wortmann, J. Hong, S. Zhou, A. J. Bornschlegl, J. Haffner-Schirmer, V. M. L. Corre, T. Heumüller, A. Osvet, B. P. Rand, L. Lüer, C. J. Brabec, *Adv. Energy Mater.* **2025**, *15*, 2502787, https://doi.org/10.1002/aenm.202502787.

[45] D. Liu, M. K. Gangishetty, T. L. Kelly, *J. Mater. Chem. A.* **2014**, *2*, 19873–19881, https://doi.org/10.1039/C4TA02637C.

[46] W. Yan, Y. Li, S. Ye, Y. Li, H. Rao, Z. Liu, S. Wang, Z. Bian, C. Huang, *Nano Res.* **2016**, *9*, 1600–1608, https://doi.org/10.1007/s12274-016-1054-5.

[47] D. Döhler, P. Büttner, F. Scheler, D. Thiel, B. Puscher, S. Bochmann, J. Mitrovic, P. P. Boix, D. M. Guldi, I. Mínguez-Bacho, J. Bachmann, *ACS Appl. Energy Mater.* **2022**, *5*, 11977–11986, https://doi.org/10.1021/acsaem.2c00870

[48] P. Büttner, D. Döhler, S. Korenko, S. Möhrlein, S. Bochmann, N. Vogel, I. Mínguez-Bacho, J. Bachmann, *RSC Adv.* **2020**, *10*, 28225–28231, https://doi.org/10.1039/D0RA04123H

[49] J. Zhang, B. Liu, Z. Liu, J. Wu, S. Arnold, H. Shi, T. Osterrieder, J. A. Hauch, Z. Wu, J. Luo, J. Wagner, C. G. Berger, T. Stubhan, F. Schmitt, K. Zhang, M. Sytnyk, T. Heumueller, C. M. Sutter-Fella, I. M. Peters, Y. Zhao, C. J. Brabec, *Adv. Energy Mater.* **2023**, *13*, 2302594, https://doi.org/10.1002/aenm.202302594.

[50] J. Zhang, J. Wu, A. Barabash, T. Du, S. Qiu, V. M. Le Corre, Y. Zhao, K. Zhang, F. Schmitt, Z. Peng, J. Tian, C. Li, C. Liu, T. Heumueller, L. Lüer, J. A. Hauch, C. J. Brabec, *Energy Environ. Sci.* **2024**, *17*, 5490–5499, https://doi.org/10.1039/D4EE01432D

[51] F. Hilpert, P.-C. Liao, E. Franz, V. M. Koch, L. Fromm, E. Topraksal, A. Görling, A.-S. Smith, M. K. S. Barr, J. Bachmann, O. Brummel, J. Libuda, *ACS Appl. Mater. Interfaces* **2023**, *15*, 19536–19544, https://doi.org/10.1021/acsami.2c16943.

[52] P. E. Hansen, *Prog. Nucl. Magn. Reson. Spectrosc.* **1981**, *14*, 175–295, https://doi.org/10.1016/0079-6565(81)80001-5.

[53] M. R. Bendall, R. E. Gordon, *J. Magn. Reson.* **1983**, *53*, 365–385.

[54] D. G. Cory, W. M. Ritchey, *J. Magn. Reson.* **1988**, *80*, 128–132.

[55] M. Shirazi, W. M. M. Kessels, A. A. Bol, *Phys. Chem. Chem. Phys.* **2018**, *20*, 16861–16875, https://doi.org/10.1039/C8CP00210J.

[56] R. W. G. Wyckoff, *Crystal Structures* , Second edition. Interscience Publishers, New York .**1963**, *1*, pp. 239–444

[57] J. Wang, R. M. Wolf, J. W. Caldwell, P. A. Kollman, D. A. Case, *J. Comput. Chem.* **2004**, *25*, 1157–1174, https://doi.org/10.1002/jcc.20035.

[58] P. Li, L. F. Song, K. M. Merz, *J. Phys. Chem. B* **2015**, *119*, 883–895, https://doi.org/10.1021/jp505875v.

[59] S. L. Mayo, B. D. Olafson, W. A. Goddard, *J. Phys. Chem.* **1990**, *94*, 8897–8909, https://doi.org/10.1021/j100389a010.

[60] P. Giannozzi, O. Andreussi, T. Brumme, O. Bunau, M. Buongiorno Nardelli, M. Calandra, R. Car, C. Cavazzoni, D. Ceresoli, M. Cococcioni, N. Colonna, I. Carnimeo, A. Dal Corso, S. De Gironcoli, P. Delugas, R. A. DiStasio, A. Ferretti Jr., A. Floris, G. Fratesi, G. Fugallo, R. Gebauer, U. Gerstmann, F. Giustino, T. Gorni, J. Jia, M. Kawamura, H.-Y. Ko, A. Kokalj, E. Küçükbenli, M. Lazzeri, et al, *J. Phys. Condens. Matter* **2017**, *29*, 465901, https://doi.org/10.1088/1361-648X/aa8f79.

[61] P. Giannozzi, S. Baroni, N. Bonini, M. Calandra, R. Car, C. Cavazzoni, D. Ceresoli, G. L. Chiarotti, M. Cococcioni, I. Dabo, A. Dal Corso, S. Fabris, G. Fratesi, S. de Gironcoli, R. Gebauer, U. Gerstmann, C. Gougoussis, A. Kokalj, M. Lazzeri, L. Martin-Samos, N. Marzari, F. Mauri, R. Mazzarello, S. Paolini, A. Pasquarello, L. Paulatto, C. Sbraccia, S. Scandolo, G. Sclauzero, A. P. Seitsonen, et al, *J. Phys. Condens. Matter* **2009**, *21*, 395502, https://doi.org/10.1088/0953-8984/21/39/395502.

[62] P. Giannozzi, O. Baseggio, P. Bonfà, D. Brunato, R. Car, I. Carnimeo, C. Cavazzoni, S. de Gironcoli, P. Delugas, F. Ferrari Ruffino, A. Ferretti, N. Marzari, I. Timrov, A. Urru, S. Baroni, *J. Chem. Phys.* **2020**, *152*, 154105, https://doi.org/10.1063/5.0005082.

[63] H. Zakaryan, V. M. Aroutiounian, *Sensors and Transducers* **2017**, *212*, 50–56.

[64] M. Melle-Franco, G. Pacchioni, *Surf. Sci.* **2000**, *461*, 54–66, https://doi.org/10.1016/S0039-6028(00)00528-8.

[65] G. Santarossa, K. Hahn, A. Baiker, *Langmuir* **2013**, *29*, 5487–5499, https://doi.org/10.1021/la400313a.

[66] Structure taken from: "DFT optimized crystal structures of inorganic and hybrid halide perovskites", latest release 2019, https://github.com/WMD-group/hybrid-perovskites (accessed on 27.05.2025).

[67] H. J. Monkhorst, J. D. Pack, *Phys. Rev. B* **1976**, *13*, 5188–5192, https://doi.org/10.1103/PhysRevB.13.5188.

[68] J. P. Perdew, A. Zunger, *Phys. Rev. B* **1981**, *23*, 5048–5079, https://doi.org/10.1103/PhysRevB.23.5048.

[69] M. J. van Setten, M. Giantomassi, E. Bousquet, M. J. Verstraete, D. R. Hamann, X. Gonze, G.-M. Rignanese, *Comp. Phys. Comm.* **2018**, *226*, 39–54, https://doi.org/10.1016/j.cpc.2018.01.012.

[70] D. R. Hamann, *Phys. Rev. B* **2013**, *88*, 085117, https://doi.org/10.1103/PhysRevB.88.085117.

[71] T. H. Fischer, J. Almlof, *J. Phys. Chem.* **1992**, *96*, 9768–9774, https://doi.org/10.1021/j100203a036.

[72] A. M. Askar, G. M. Bernard, B. Wiltshire, K. Shankar, V. K. Michaelis, *J. Phys. Chem. C* **2017**, *121*, 1013–1024, https://doi.org/10.1021/acs.jpcc.6b10865.

[73] W. Chen, X. Yin, M. Que, H. Xie, J. Liu, C. Yang, Y. Guo, Y. Wu, W. Que, *J. Power Sources* **2019**, *412*, 118–124, https://doi.org/10.1016/j.jpowsour.2018.11.031.

[74] M. Saliba, L. Etgar, *ACS Energy Lett.* **2020**, *5*, 2886–2888, https://doi.org/10.1021/acsenergylett.0c01642.

Manuscript received: June 25, 2025
Revised manuscript received: September 17, 2025
Manuscript accepted: October 09, 2025
Version of record online: ■■, ■■